RSC Advances

PAPER

View Article Online
View Journal | View Issue

Cite this: *RSC Adv.*, 2024, **14**, 20113

Charge transport through the multiple end zigzag edge states of armchair graphene nanoribbons and heterojunctions

David M. T. Kuo

This comprehensive study investigates charge transport through the multiple end zigzag edge states of finite-size armchair graphene nanoribbons/boron nitride nanoribbons (*n*-AGNR/*w*-BNNR) junctions under a longitudinal electric field, where *n* and *w* denote the widths of the AGNRs and the BNNRs, respectively. In 13-atom wide AGNR segments, the edge states exhibit a blue Stark shift in response to the electric field, with only the long decay length zigzag edge states showing significant interaction with the red Stark shift subband states. Charge tunneling through such edge states assisted by the subband states is elucidated in the spectra of the transmission coefficient. In the 13-AGNR/6-BNNR heterojunction, notable influences on the energy levels of the end zigzag edge states of 13-AGNRs induced by BNNR segments are observed. We demonstrate the modulation of these energy levels in resonant tunneling situations, as depicted by bias-dependent transmission coefficient spectra. Intriguing nonthermal broadening of tunneling current shows a significant peak-to-valley ratio. Our findings highlight the promising potential of *n*-AGNR/*w*-BNNR heterojunctions with long decay length edge states in the realm of GNR-based single electron transistors at room temperature.

Received 5th April 2024
Accepted 18th June 2024

DOI: 10.1039/d4ra02574a

rsc.li/rsc-advances

1 Introduction

Graphene nanoribbons (GNRs) have been the subject of extensive study since the groundbreaking discovery of two-dimensional graphene in 2004 by Novoselov and Geim.[1] Known for their semiconducting phases resulting from quantum confinement, GNRs hold significant promise for next-generation electronics.[2–4] Among these, armchair GNRs (AGNRs) are particularly noteworthy due to their tunable band gaps, which are inversely proportional to their widths.[5–12] Recent research has focused on understanding the electronic properties of AGNRs under transverse electric fields, revealing transitions from semiconducting to semimetallic phases.[13–16] These transitions could be crucial for controlling plasmon propagation.

The terminal zigzag edge structures of AGNRs play a critical role in field-effect transistors (FETs), directly interfacing with the source and drain electrodes.[8,9] These structures harbor topological states (TSs), the response of which to electric fields remains poorly understood.[17,18] Wider AGNRs exhibit multiple terminal zigzag edge states in finite segments.[19,20] For instance, in 13-atom wide AGNR (13-AGNR) segments, each terminal may possess two distinct zigzag edge states, one with an exponential decay characteristic length and another with a longer characteristic length. Although the current spectra of 13-AGNR tunneling FETs have been experimentally reported, a systematic analysis of charge tunneling through the topological edge states and the subband states is lacking.[8] Meanwhile, scientists want to know how the electronic and transport properties of GNRs are changed when GNRs are embedded into h-boron nitride sheets,[16] which is a critical issue to realize GNR-based electronic circuits.[21–23]

This study aims to elucidate the electronic and transport properties of multiple end zigzag edge states in finite-size AGNRs and AGNR/boron nitride nanoribbon (BNNR) heterojunctions under longitudinal electric fields. Fig. 1 illustrates an *n*-AGNR/*w*-BNNR heterojunction, where *n* and *w* denote the widths of AGNR and BNNR, respectively. Given the challenges associated with using density functional theory (DFT) to calculate the transmission coefficient of GNR segments under electric fields,[24,25] we employ a tight-binding model and Green's function technique to compute the bias-dependent transmission coefficient.[26–28] This approach enables us to elucidate the charge transport through multiple zigzag edge states in finite 13-AGNRs and 13-AGNR/6-BNNR heterojunctions. Spectra of transmission coefficients reveal interference between subband states and long characteristic length zigzag edge states in the finite 13-AGNR structure. Furthermore, the on-off switch behavior arising from resonant tunneling between the left and right zigzag edge states of the 13-AGNR/6-BNNR heterojunction is discerned in the transmission coefficient spectra.

Department of Electrical Engineering, Department of Physics, National Central University, Chungli, 32001, Taiwan. E-mail: mtkuo@ee.ncu.edu.tw

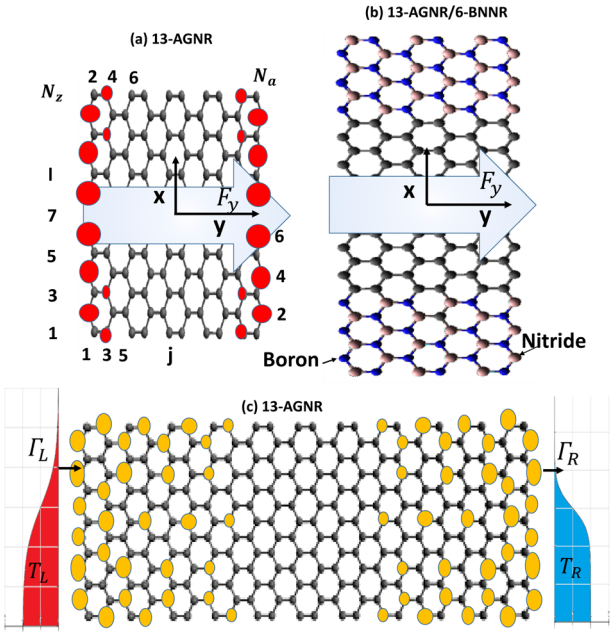

Fig. 1 (a) and (b) Schematic diagrams illustrating the armchair graphene nanoribbon (13-AGNR) and 13-AGNR/6-BNNR heterojunction under longitudinal electric fields, respectively. Schematic diagram (c) depicts the line-contacting of zigzag-edge atoms in a 13-AGNR structure to electrodes. Symbols $\Gamma_L(\Gamma_R)$ represent the electron tunneling rate between the left (right) electrode and the leftmost (rightmost) atoms at the zigzag edges, and $T_L(T_R)$ denotes the equilibrium temperature of the left (right) electrode. The probability densities of the zigzag edge states with short and long characteristic lengths in 13-AGNR segments without electric fields are plotted in (a) and (c), respectively. The radius of the circle represents the magnitude of the probability density.

Intriguingly, nonthermal broadening tunneling current exhibits a large peak-to-valley ratio, which is highly useful for applications such as single-electron transistors at room temperature.

2 Calculation methodology

To investigate the transport properties of 13-AGNR and 13-AGNR/6-BNNR heterojunctions connected to the electrodes, we employ a combination of the tight-binding model and the Green's function technique. The system Hamiltonian depicted in Fig. 1(c) is written as $H = H_0 + H_{GNR}$, where

$$H_0 = \sum_k \varepsilon_k a_k^\dagger a_k + \sum_k \varepsilon_k b_k^\dagger b_k + \sum_\ell \sum_k V_{k,\ell j}^{L} d_{\ell j}^\dagger a_k + \sum_\ell \sum_k V_{k,\ell j}^{R} d_{\ell j}^\dagger b_k + \text{h.c.} \quad (1)$$

The first two terms of eqn (1) describe the free electrons in the left and right metallic electrodes. $a_k^\dagger(b_k^\dagger)$ creates an electron of with momentum k and energy ε_k in the left (right) electrode. $V_{k,\ell j=1}^{L}(V_{k,\ell j=N_a}^{R})$ describes the coupling between the left (right) lead with its adjacent atom in the ℓ-th row.

$$H_{GNR} = \sum_{\ell,j} E_{\ell j} d_{\ell j}^\dagger d_{\ell j} - \sum_{\ell,j}\sum_{\ell',j'} t_{(\ell j),(\ell' j')} d_{\ell j}^\dagger d_{\ell' j'} + \text{h.c}, \quad (2)$$

Here, $E_{\ell j}$ represents the on-site energy of the orbital in the ℓ-th row and j-th column. The operators $d_{\ell j}^\dagger$ and $d_{\ell j}$ create and annihilate an electron at the atom site denoted by (ℓ,j). The parameter $t_{(\ell j),(\ell' j')}$ characterizes the electron hopping energy from site (ℓ',j') to site (ℓ,j). For the tight-binding parameters of n-AGNR/w-BNNR, we assign $E_B = 2.329$ eV, $E_N = -2.499$ eV, and $E_C = 0$ eV to boron, nitride, and carbon atoms, respectively. We neglect variations in electron hopping strengths between different atoms for simplicity.[29,30] We set $t_{(\ell j),(\ell' j')} = t_{pp\pi} = 2.7$ eV for the nearest-neighbor hopping strength. Additionally, the effect of electric field F_y is included by the electric potential $U = eF_y y$ on $E_{\ell,j}$, where $F_y = V_y/L_a$, with V_y as the applied bias and L_a as the length of the AGNR segment.

We calculate the bias-dependent transmission coefficient $\mathcal{T}_{LR}(\varepsilon)$ using the formula: $\mathcal{T}_{LR}(\varepsilon) = 4Tr[\Gamma_L(\varepsilon)G^r(\varepsilon)\Gamma_R(\varepsilon)G^a(\varepsilon)]$,[26] where $\Gamma_L(\varepsilon)$ and $\Gamma_R(\varepsilon)$ denote the tunneling rate (in energy units) at the left and right leads, respectively, and $G^r(\varepsilon)$ and $G^a(\varepsilon)$ are the retarded and advanced Green's functions of the GNRs, respectively. In terms of tight-binding orbitals, $\Gamma_\alpha(\varepsilon)$ and Green's functions are matrices. The expression for $\Gamma_{L(R)}(\varepsilon)$ is derived from the imaginary part of the self-energies, denoted as $\sum_{L(R)}^{r}(\varepsilon)$, and is given by $\Gamma_{L(R)}(\varepsilon) = -\text{Im}(\sum_{L(R)}^{r}(\varepsilon)) = \pi\sum_k \left|V_{k,\ell j}^{L(R)}\right|^2 \delta(\varepsilon - \varepsilon_k)$, where $V_{k,\ell j=1}^{L}$ and $V_{k,\ell j=N_a}^{R}$ denote the coupling strengths between the left and right metallic electrodes with their adjacent atoms (refer to Fig. 1). In the context of metals such as gold, where the density of states remains approximately constant near the Fermi energy, the wide-band limit serves as a suitable approximation. In this limit, the energy-dependent tunneling rates, $\Gamma_{L(R)}(\varepsilon)$, are replaced by constant matrices denoted as $\Gamma_{L(R)}$.[26] However, it's important to note that in some cases, only the diagonal entries of $\Gamma_{L(R)}$ are non-zero. Additionally, if one adopts the alternative definition of $\Gamma_{L(R)}(\varepsilon) = -i[\sum_{L(R)}^{r}(\varepsilon) - \sum_{L(R)}^{a}(\varepsilon)]$, the factor "4" in the transmission coefficient is reset to one.[31–33] Notably, $\Gamma_{L(R)}$ calculated within the wide-band limit can effectively replicate the transmission coefficient curves of graphene nanoribbon superlattices obtained using the surface Green's function method, as demonstrated in ref. 32 and 33.

3 Results and discussion

Before examining the effects of electric fields on the electronic and transport properties of end zigzag edge states of 13-AGNR and 13-AGNR/6-BNNR structures, we first present the electronic structures of these two configurations in Fig. 2(a) and (b), respectively. Both structures maintain semiconductor properties with direct band gaps. Specifically, the 13-AGNR and 13-AGNR/6-BNNR exhibit band gaps of 0.714 eV and 0.722 eV, respectively, consistent with values calculated by the DFT method.[30] It's noteworthy that the electronic structures of 13-AGNR/w-BNNR remain unchanged when $w \geq 6$. This suggests that a 6-BNNR width is sufficient to model 13-AGNR embedded within an h-BN sheet. Although the impact of BNNR on the band gaps of 13-AGNRs is not significant, we will demonstrate

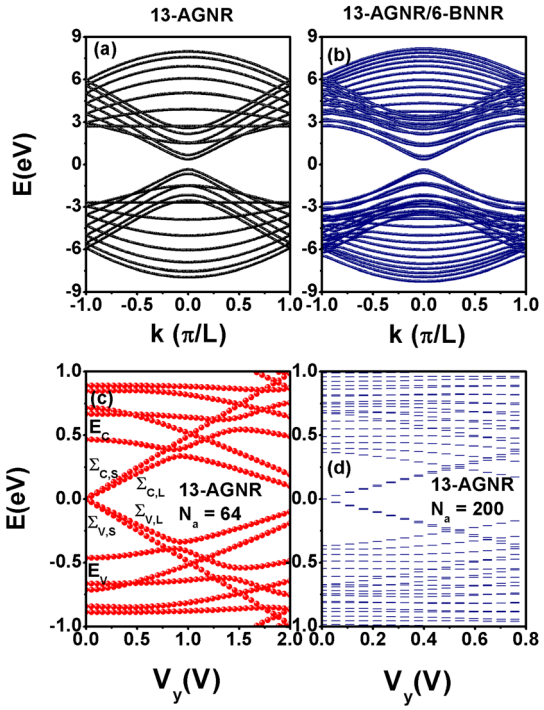

Fig. 2 Electronic structures of 13-AGNR and 13-AGNR/6-BNNR structures. (a) 13-AGNR structure and (b) 13-AGNR/6-BNNR structure. Energy levels of 13-AGNRs as functions of applied voltage V_y for two different N_a values. (c) $N_a = 64$ ($L_a = 6.67$ nm) and (d) $N_a = 200$ ($L_a = 21.16$ nm). Note that the energy levels are plotted with respect to the Fermi energy E_F, which is set as zero throughout this article.

later that BNNR structures have a notable effect on the end zigzag edge states of 13-AGNRs.

3.1 13-AGNR segments under an electric field

To elucidate the end zigzag edge states of 13-AGNRs, we analyze the energy spectra of 13-AGNR segments under an electric field. Fig. 2(c) and (d) illustrate the energy levels of 13-AGNR segments with $N_a = 64$ ($L_a = 6.67$ nm) and $N_a = 200$ ($L_a = 21.16$ nm) as functions of V_y. In the absence of an electric field, four energy levels exist between E_C and E_V, representing the subband states as depicted in Fig. 2(c). These levels are denoted as $\Sigma_{C,S}$, $\Sigma_{C,L}$, $\Sigma_{V,S}$, and $\Sigma_{V,L}$. Here, C and V distinguish the energy levels above or below the Fermi energy, while S and L represent short and long decay characteristic lengths, respectively. These levels arise from the formation of bonding and antibonding states between the left and right TSs ($\Psi_{L,S(L)}$ and $\Psi_{R,S(L)}$), as noted in ref. 19. For $N_a = 64$, $\Sigma_{C(V),L} = \pm 7.13$ meV and $\Sigma_{C(V),S} = 0$. For $N_a = 200$, $\Sigma_{C(V),L} = \pm 7$ μeV and $\Sigma_{C(V),S} = 0$. When considering $N_a = 200$, E_C and E_V are 0.3668 eV and −0.3668 eV, respectively, which closely correspond to the minimum conduction subband and the maximum valence subband of infinitely long 13-AGNRs shown in Fig. 2(a). Notably, in Fig. 2(c) and (d), we observe a blue Stark shift of TSs and a red Stark shift of the subband states. Consequently, the energy levels of end zigzag edge states cross the subband states. With increasing N_a, the applied bias inducing such a crossing is shifted toward lower bias, as observed in Fig. 2(d). Note that the Stark shift of energy levels for graphene nanoribbon (GNR) segments (or graphene quantum dots) responds sensitively to the applied electric fields, with directionality playing a crucial role.[34,35] Particularly, when transverse electric fields (F_x) are introduced to armchair graphene nanoribbons (AGNRs), we observe an intriguing semiconductor-to-semimetal transition in the electronic structures.[13,15]

To further comprehend the charge transport through these topological states ($\Psi_{L(R),S}$ and $\Psi_{L(R),L}$), we plot the transmission coefficient $\mathcal{T}_{LR}(\varepsilon)$ of a 13-AGNR segment with $N_a = 64$ for various V_y values in Fig. 3(a)–(c). As depicted in Fig. 3(a), the peak labeled by Σ_0 arises from $\Sigma_{C,L}$ and $\Sigma_{V,L}$, rather than $\Sigma_{C,S}$ and $\Sigma_{V,S}$, as their wave functions ($\Psi_{L,S}$ and $\Psi_{R,S}$) are highly localized on the end zigzag edges (see Fig. 1(a)). With the application of bias voltage V_y in Fig. 3(b), the probability for charge tunneling through these topological states diminishes significantly due to the off-resonance energy levels of $\Psi_{L,L}$ and $\Psi_{R,L}$. Upon reaching $V_y = 0.918$ V, two peaks labeled $\varepsilon_{C(V),B}$ and $\varepsilon_{C(V),A}$ emerge due to the interference between the end zigzag edge states $\Sigma_{C(V),L}$ and the subband states $E_{C(V)}$, as seen in Fig. 3(c). The peak at $\varepsilon_{C(V),B}$ can be interpreted as charge tunneling through the long decay length edge state under the subband states ($E_{C(V)}$) assisted procedure. Fig. 3(d) illustrates the contact effect on this interference phenomenon. As Γ_t decreases, the resolution between the peaks ($\varepsilon_{C,B}$ and $\varepsilon_{C,A}$) becomes more distinct. For $\Gamma_t = 90$ meV, the interference pattern resembles Fano interference. The probability distributions of the peaks labeled $\varepsilon_{C,B}$ and $\varepsilon_{C,A}$ are shown in Fig. 3(e) and (f), respectively. It is evident that $\varepsilon_{C(V),B}$ and $\varepsilon_{C(V),A}$ correspond to

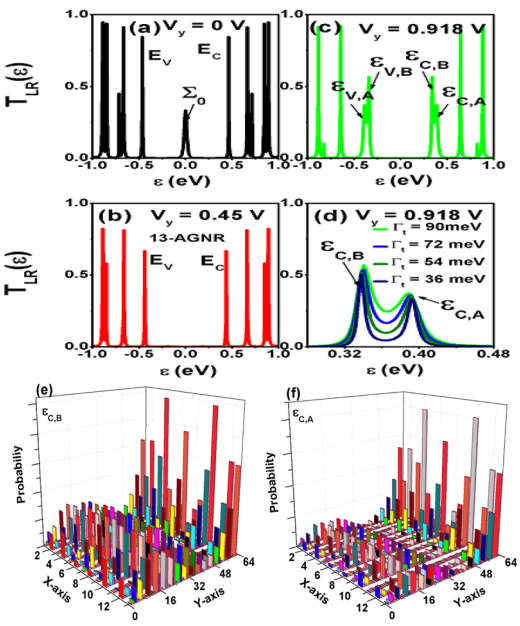

Fig. 3 Transmission coefficients $\mathcal{T}_{LR}(\varepsilon)$ of 13-AGNRs with $N_a = 64$ for various V_y values at $\Gamma_t = 0.09$ eV. Panels (a), (b), and (c) correspond to $V_y = 0$, $V_y = 0.45$ V, and $V_y = 0.918$ V, respectively. Panel (d) shows the $\mathcal{T}_{LR}(\varepsilon)$ for various Γ_t values at $V_y = 0.918$ V. Panels (e) and (f) depict probability densities of $\varepsilon_{C,B} = 0.337$ eV and $\varepsilon_{C,A} = 0.393$ eV in a 13-AGNR segment with $N_a = 64$ and $V_y = 0.918$ V.

constructive and destructive interferences between the wave function of the conduction (valence) subband state and the wave function of the right (left) edge state with a long characteristic length ($\Psi_{R(L),L}$). Although many theoretical efforts predict the existence of topological states of GNRs,[10–12] revealing the quantum interference between the TSs and the subband states based on the tunneling spectra of GNR-based electronic devices remains a challenge.[8,9]

3.2 13-AGNR/6-BNNR segments under an electric field

Considering the influence of h-BN on the electronic and transport properties of 13-AGNRs, we present the energy levels of 13-AGNR/6-BNNR structures as functions of applied V_y for various N_a values in Fig. 4(a)–(c). In the gap region of the 13-AGNR/6-BNNR structure (refer to Fig. 2(b)), there are still four energy levels present ($\Sigma_{C,S}$, $\Sigma_{C,L}$, $\Sigma_{V,S}$, and $\Sigma_{V,L}$). Unlike the multiple end zigzag edge states of 13-AGNRs, the multiple zigzag edge states of finite 13-AGNR/6-BNNR heterojunctions are insensitive to variations in N_a, remaining nearly fixed at specific energy levels. For instance, at $N_a = 44$, we have $\Sigma_{C,S} = 76.4$ meV ($\Sigma_{V,S} = -81.7$ meV) and $\Sigma_{C,L} = 0.253$ eV ($\Sigma_{V,L} = -0.268$ eV). Similarly, at $N_a = 64$, we observe $\Sigma_{C,S} = 76.4$ meV ($\Sigma_{V,S} = -81.7$ meV) and $\Sigma_{C,L} = 0.249$ eV ($\Sigma_{V,L} = -0.263$ eV). This indicates that $\Sigma_{C,S}$, $\Sigma_{C,L}$, $\Sigma_{V,S}$, and $\Sigma_{V,L}$ are not determined by the wave function overlaps between the left and right TSs. In finite 13-AGNR/6-BNNR heterojunctions, BNNRs have the left boron atom zigzag edge terminal and the right nitride atom zigzag edge terminal (see Fig. 1(b)). The energy levels of $\Sigma_{C,S}$, $\Sigma_{C,L}$, $\Sigma_{V,S}$, and $\Sigma_{V,L}$ are significantly influenced by the energy levels of boron and nitride atoms.

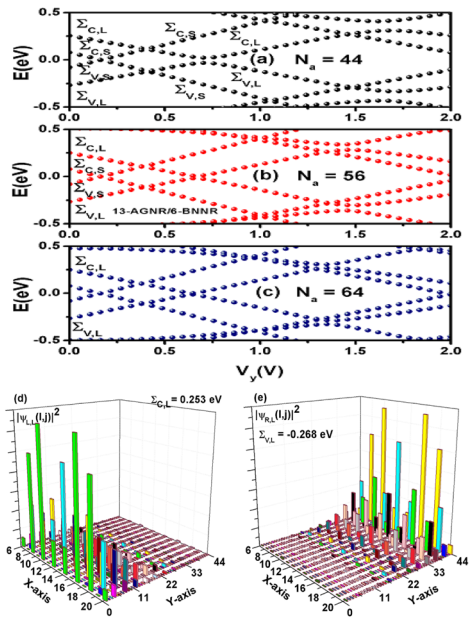

Fig. 4 Energy levels of 13-AGNR/6-BNNR heterojunction as functions of V_y for various N_a. Panels (a), (b), and (c) correspond to $N_a = 44$ ($L_a = 4.54$ nm), $N_a = 56$ ($L_a = 5.82$ nm), and $N_a = 64$ ($L_a = 6.67$ nm), respectively. Probability densities of 13-AGNR/6-BNNR heterojunction with $N_a = 44$ ($L_a = 4.54$ nm) at $V_y = 0$. Panels (d) and (e) depict the probability densities of $\Sigma_{C,L}$ and $\Sigma_{V,L}$, respectively.

Fig. 4(a)–(c) indicate that the multiple zigzag edge states of 13-AGNR/6-BNNR exhibit a linear function of the electric field. In the high bias region ($V_y > 1$ V), the interaction spectra resulting from the multiple end zigzag edge states and the subband states can be reproduced, akin to the interference scenario observed in 13-AGNRs (Fig. 2(c) and (d)). Before calculating the transmission coefficient of 13-AGNR/6-BNNR heterojunction, we plot the probability densities of $\Sigma_{C,L}$ and $\Sigma_{V,L}$ at $V_y = 0$ and $N_a = 44$ in Fig. 4(d) and (e), respectively. From the probability distributions of $\Sigma_{C,L}$ and $\Sigma_{V,L}$, it is evident that charges are confined within the 13-AGNR segment, demonstrating that BNNRs act as potential barriers. Additionally, $\Sigma_{C,L}(\Sigma_{V,L})$ is determined by the unoccupied carbon–nitride antibonding state (occupied carbon–boron bonding state).[36,37]

The maximum probability of $\Sigma_{C,L}(\Sigma_{V,L})$ occurs at sites labeled by $\ell = 10$ and $\ell = 16$ at $j = 1$ ($\ell = 10$ and $\ell = 16$ at $j = 44$). The probability distribution of $\Sigma_{C,L}(\Sigma_{V,L})$ along the y direction exhibits a long decay length, spanning several benzene sizes, yet its probability density near the right (left) electrode sites is minimal. This indicates that the wave function of $\Sigma_{C,L}(\Sigma_{V,L})$ is weakly coupled to the right (left) electrode. The asymmetrical coupling to the left and right electrodes for the wave function of $\Sigma_{C,L}(\Sigma_{V,L})$ hinders charge transport through this energy level.

We now present the calculated transmission coefficient of the 13-AGNR/6-BNNR heterojunction with $N_a = 44$ for various applied bias V_y values at $\Gamma_t = 90$ meV in Fig. 5. In Fig. 5(a) and (b), the charge transport through $\Sigma_{C,L}$ and $\Sigma_{V,L}$ is hindered due

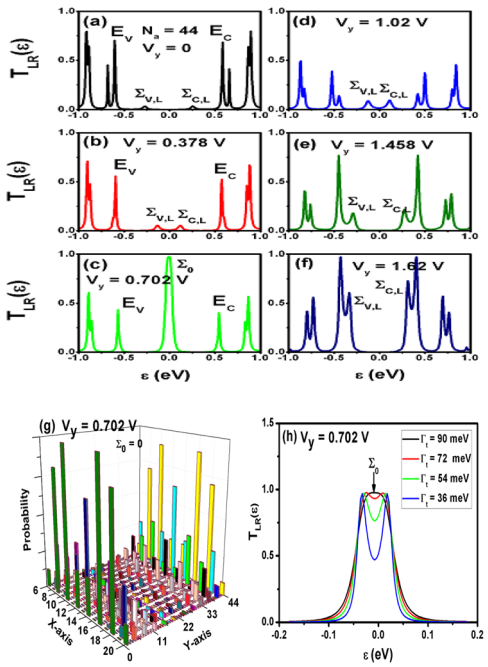

Fig. 5 Transmission coefficient $\mathcal{T}_{LR}(\varepsilon)$ of the 13-AGNR/6-BNNR heterojunction with $N_a = 44$ for various V_y values at $\Gamma_t = 90$ meV. Panels (a) through (f) correspond to V_y values of 0, 0.378 V, 0.702 V, 1.02 V, 1.458 V, and 1.62 V, respectively. Panel (g) displays the probability distribution of $\Sigma_0 = 0$ at $V_y = 0.702$ V. Panel (h) shows the transmission coefficient $\mathcal{T}_{LR}(\varepsilon)$ as functions of ε for various Γ_t values at $V_y = 0.702$ V.

to the very weak coupling strength between the electrodes and the zigzag edge states. However, a significant peak of Σ_0 occurs for ε near the Fermi energy at $V_y = 0.702$ V in Fig. 5(c). For $V_y =$ 1.02 V and $V_y = 1.458$ V, the peaks for charge transport through $\Sigma_{C,L}$ and $\Sigma_{V,L}$ are shifted away from the Fermi energy, as shown in Fig. 5(d) and (e). A notable enhancement of charge transport through $\Sigma_{C,L}$ and $\Sigma_{V,L}$ is observed for $V_y = 1.62$ V, which is attributed to the assistance from subband states.

The transmission coefficient of Σ_0 shown in Fig. 3(c) is attributed to the alignment between $\Sigma_{C,L}$ and $\Sigma_{V,L}$. We plot the probability distribution of $\Sigma_0 = 0$ in Fig. 5(g). The symmetrical probability distribution explains the alignment of $\Sigma_{C,L}$ and $\Sigma_{V,L}$. As these two levels approach alignment, their wave functions $\Psi_{C,\mathrm{L}(\ell,j)}$ and $\Psi_{V,\mathrm{R}(\ell,j)}$ generate constructive and destructive superpositions, forming the two splitting peaks. To resolve these two peaks, we present the transmission coefficient $\mathcal{T}_{\mathrm{LR}}(\varepsilon)$ for various Γ_t values in Fig. 5(h). The results in Fig. 5(h) indicate that the transmission coefficient is affected not only by the applied voltage but also by the contact property between the electrodes and the 13-AGNR/6-BNNR heterojunctions. For weak $\Gamma_t = 36$ meV, we observe two separated peaks.

3.3 Tunneling current through the zigzag edge states of 13-AGNR/6-BNNR heterojunctions

In this subsection, we investigate the tunneling current through the end zigzag edge states with long decay length, utilizing the effective 2-site Hubbard model.[38] The transmission coefficient curves depicted in Fig. 3(d) and 5(h) can be faithfully replicated by the effective 2-site Hubbard model, as the zigzag edge states are well-separated from the subband states under low applied bias, and their wave functions are localized.[27] The tunneling current is determined by the expression:

$$J = \frac{-2e}{h}\int \mathrm{d}\varepsilon\ \mathcal{T}_{2\text{-site}}(\varepsilon)[f_{\mathrm{L}}(\varepsilon) - f_{\mathrm{R}}(\varepsilon)] \quad (3)$$

where $f_{\mathrm{L(R)}}(\varepsilon)$ denotes the Fermi distribution function of the left (right) electrode with the chemical potential $\mu_{\mathrm{L(R)}} = E_{\mathrm{F}} \mp eV_y/2$. The bias-dependent transmission coefficient, $\mathcal{T}_{2\text{-site}}(\varepsilon)$, includes one-particle, two-particle, and three-particle correlation functions in the Coulomb blockade region, computed self-consistently.[39] Furthermore, the bias-independent intra-site (U_0) and inter-site (U_1) Coulomb interactions are computed using $U_n = \frac{1}{4\pi\epsilon_0}\sum_{i,j}\left|\Psi_{C(V),L}(\mathbf{r}_i)\right|^2\left|\Psi_{C(V),L}(\mathbf{r}_j)^2\right|\frac{1}{|\mathbf{r}_i - \mathbf{r}_j|}$ with the dielectric constant $\varepsilon_0 = 4$, and $U_{\mathrm{cc}} = 4$ eV at $i = j$. U_{cc} arises from the two-electron occupation in each p_z orbital. In Fig. 6, the non-interaction curve corresponds to the case depicted in Fig. 4(c). The inset of Fig. 6 illustrates charge transport in the Coulomb blockade region, where $\varepsilon_{C,L} = \Sigma_{C,L} - \eta eV_y + i\Gamma_{e,\mathrm{L}}$ and $\varepsilon_{V,L} = \Sigma_{V,L} + \eta eV_y + i\Gamma_{e,\mathrm{R}}$. Here, $\eta eV_y = 0.336eV_y$ represents the orbital offset terms induced by the applied voltage (V_y), and $\Gamma_{e,\mathrm{L}} = \Gamma_{e,\mathrm{R}} = \Gamma_{e,t}$ represents the effective tunneling rate of end zigzag states in the 2-site model, determined by Γ_t and the wave functions of the edge states $\Psi_{C(V),\mathrm{L}}$.

The first peak of the red curve, calculated at temperature $T =$ 300 K and labeled ε_1, corresponds to the charge transfer from

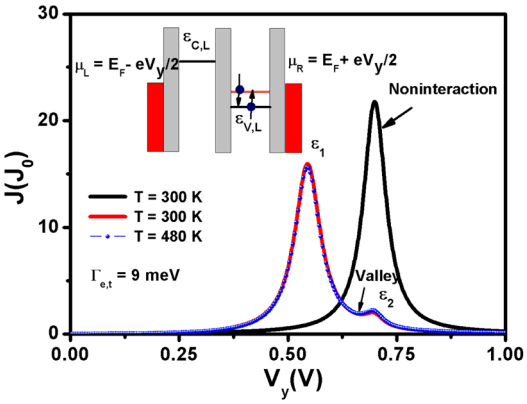

Fig. 6 Tunneling current through the end zigzag edge state with a long decay length of the 13-AGNR/6-BNNR heterojunction with $N_a = 64$. Energy levels are defined as $\varepsilon_{C,L} = \Sigma_{C,L} - 0.366eV_y + i\Gamma_{e,\mathrm{L}}$ and $\varepsilon_{V,L} = \Sigma_{V,L} + 0.366eV_y + i\Gamma_{e,\mathrm{R}}$. Other physical parameters include $\Sigma_{C,L} =$ 0.249 eV, $\Sigma_{V,L} = -0.263$ eV, intra-site Coulomb interaction $U_0 = 155$ meV, inter-site Coulomb interaction $U_1 = 42$ meV, and inter-site electron hopping strength $t_{\mathrm{LR}} = 7.13$ meV. We have $\Gamma_{e,\mathrm{L}} = \Gamma_{e,\mathrm{R}} = \Gamma_{e,t} =$ 9 meV, $E_{\mathrm{F}} = 0$, and $J_0 = 0.773$ nA.

$\varepsilon_{V,L} + U_0$ to $\varepsilon_{C,L}$ when these two energy levels align. The second peak, ε_2, corresponds to electron transfer between $\varepsilon_{V,L}$ and $\varepsilon_{C,L}$. However, the tunneling current for such a procedure is significantly suppressed due to electron Coulomb interactions. The blue curve with markers is calculated at $T = 480$ K. Distinguishing between the red and blue curves in the entire applied voltage region is challenging, illustrating the nonthermal broadening effect of the tunneling current. Additionally, the peak-to-valley ratio reaches 8.7. The results presented in Fig. 6 demonstrate that the edge states with long decay length act as effective single charge filters at room temperature, suggesting their potential application in single-electron transistors at room temperature.[40] Traditional single electron transistors formed by a single quantum dot exhibit temperature-dependent tunneling current spectra,[41–43] where the peak-to-valley ratio of tunneling current tends to decrease with increasing temperature. Our study demonstrates that the tunneling current through the zigzag edge states of 13-AGNR/6-BNNR heterojunctions maintains temperature stability, a significant advantage for practical applications.

4 Conclusion

In this study, we investigated the charge transport properties through the multiple end zigzag edge states of both 13-AGNR and 13-AGNR/6-BNNR heterojunctions under longitudinal electric fields, employing the tight-binding model and Green's function technique. For 13-AGNRs, we elucidated the distinct blue Stark shift behaviors exhibited by the zigzag edge states with short and long decay lengths in response to electric fields. We found that the latter can significantly interact with the subband states, thereby unveiling the mechanism of charge transport through the long decay length zigzag edge states assisted by the subband states, as evidenced by the spectra of the transmission coefficient.

Concerning 13-AGNR/6-BNNR heterojunctions, we observed that the energy levels of the end zigzag edge states of 13-AGNRs are notably influenced by the presence of BNNRs rather than their lengths. Even in long 13-AGNR/6-BNNR segments, $\Sigma_{C,L}$ exhibits a significant orbital offset from $\Sigma_{V,L}$. We further revealed a remarkable resonant tunneling process for charge transfer between $\Sigma_{C,L}$ and $\Sigma_{V,L}$ through the bias-dependent transmission coefficient analysis.

Moreover, employing a 2-site Hubbard model, we analyzed the tunneling current through the end zigzag edge states of 13-AGNR/6-BNNR heterojunctions within the Coulomb blockade region. Our results demonstrate that these edge states function effectively as single charge filters at room temperature, exhibiting a high peak-to-valley ratio of tunneling current with a nonthermal broadening effect, as illustrated in Fig. 6. This unique characteristic suggests promising applications of 13-AGNR/6-BNNR heterojunctions in single electron transistors operating at room temperature.

Data availability

The data presented in this study are available upon reasonable request.

Conflicts of interest

There are no conflicts to declare.

Acknowledgements

This work was supported by the National Science and Technology Council, Taiwan under Contract No. MOST 107-2112-M-008-023MY2.

References

1 K. S. Novoselov, A. K. Geim, S. V. Morozov, D. Jiang, Y. Zhang, S. V. Dubonos, I. V. Grigorieva and A. A. Firsov, Electric field effect in atomically thin carbon films, *Science*, 2004, **306**, 666.
2 J. Haskins, A. Kinaci, C. Sevik, H. Sevincli, G. Cuniberti and T. Cagin, Control of Thermal and Electronic Transport in Defect-Engineered Graphene Nanoribbons, *ACS Nano*, 2011, **5**, 3779–3787.
3 P. H. Chang, M. S. Bahramy, N. Nagaosa and B. K. Nikolic, Giant Thermoelectric Effect in Graphene-Based Topological Insulators with Heavy Adatoms and Nanopores, *Nano Lett.*, 2014, **14**, 3779–3784.
4 H. M. Wang, H. S. Wang, C. X. Ma, L. X. Chen, C. X. Jiang, C. Chen, X. M. Xie, A. P. Li and X. R. Wang, Graphene nanoribbons for quantum electronics, *Nat. Rev. Phys.*, 2021, **3**, 791.
5 J. Cai, P. Ruffieux, R. Jaafar, M. Bieri, T. Braun, S. Blankenburg, M. Muoth, A. P. Seitsonen, M. Saleh, X. Feng, K. Mullen and R. Fasel, Atomically precise bottom-up fabrication of graphene nanoribbons, *Nature*, 2010, **466**, 470.
6 J. Z. Liu, B. W. Li, Y. Z. Tan, A. Giannakopoulos, C. Sanchez-Sanchez, D. Beljonne, P. Ruffieux, R. Fasel, X. L. Feng and K. Mullen, Toward Cove-Edged Low Band Gap Graphene Nanoribbons, *J. Am. Chem. Soc.*, 2015, **137**, 6097.
7 Y. C. Chen, T. Cao, C. Chen, Z. Pedramraz, D. Haberer, D. G. de Oteyza, R. Fischer, S. G. Louie and M. F. Crommie, Molecular bandgap engineering of bottom-up synthesized graphene nanoribbon heterojunctions, *Nat. Nanotechnol.*, 2015, **10**, 156.
8 J. P. Llinas, A. Fairbrother, G. Borin Barin, W. Shi, K. Lee, S. Wu, B. Y. Choi, R. Braganza, J. Lear, N. Kau, *et al.*, Short-channel field-effect transistors with 9-atom and 13-atom wide graphene nanoribbons, *Nat. Commun.*, 2017, **8**, 633.
9 P. H. Jacobse, A. Kimouche, T. Gebraad, M. M. Ervasti, J. M. Thijssen, P. Liljeroth and I. Swart, Electronic components embedded in a single graphene nanoribbon, *Nat. Commun.*, 2017, **8**, 119.
10 D. J. Rizzo, G. Veber, J. W. Jiang, R. McCurdy, T. Bronner, T. Cao, T. Chen, S. G. Louie, F. R. Fischer and M. F. Crommie, Inducing metallicity in graphene nanoribbons via zero-mode superlattices, *Science*, 2020, **369**, 1597.
11 Q. Sun, Y. Yan, X. L. Yao, K. Mullen, A. Narita, R. Fasel and P. Ruffieux, Evolution of the Topological Energy Band in Graphene Nanoribbons, *J. Phys. Chem. Lett.*, 2021, **12**, 8679.
12 D. J. Rizzo, J. W. Jiang, D. Joshi, G. Veber, C. Bronner, R. A. Durr, P. H. Jacobse, T. Cao, A. Kalayjian, H. Rodriguez, P. Butler, T. Chen, S. G. Louie, F. R. Fischer and M. F. Crommie, Rationally Designed Topological Quantum Dots in Bottom-Up Graphene Nanoribbons, *ACS Nano*, 2021, **15**, 20633.
13 F. Z. Zhao, T. Cao and S. G. Louie, Topological Phases in Graphene Nanoribbons Tuned by Electric Fields, *Phys. Rev. Lett.*, 2021, **127**, 166401.
14 X. Wang, Y. Q. Cui, L. Zhang and M. L. Yang, Enhanced second-order Stark effect in twisted bilayer graphene quantum dots, *Nano Res.*, 2021, **14**, 3935.
15 M. Pizzochero, N. V. Tepliakov, A. A. Mostofi and E. Kaxiras, Electrically Induced Dirac Fermions in Graphene Nanoribbons, *Nano Lett.*, 2021, **21**, 9332.
16 V. T. Nikita, M. Ruize, L. Johannes, K. Efthimios, A. M. Arash and P. Michele, Dirac Half-Semimetallicity and Antiferromagnetism in Graphene Nanoribbon/Hexagonal Boron Nitride Heterojunctions, *Nano Lett.*, 2023, **23**, 6698.
17 N. V. Tepliakov, J. Lischner, E. Kaxiras, A. A. Mostofi and M. Pizzochero, Unveiling and Manipulating Hidden Symmetries in Graphene Nanoribbons, *Phys. Rev. Lett.*, 2023, **130**, 026401.
18 M. Golor, C. Koop, T. C. Lang, S. Wessel and M. J. Schmidt, Magnetic correlations in short and narrow graphene armchair nanoribbons, *Phys. Rev. Lett.*, 2013, **111**, 085504.
19 M. P. Lopez-Sancho and M. Carmen Munoz, Topologically protected edge and confined states in finite armchair graphene nanoribbons and their junctions, *Phys. Rev. B: Condens. Matter Mater. Phys.*, 2021, **104**, 245402.

20 A. D. Zdetsis, Peculiar electronic properties of wider armchair graphene nanoribbons: Multiple topological end-states and "phase transitions", *Carbon*, 2023, **210**, 118042.
21 L. X. Chen, L. He, H. S. Wang, H. M. Wang, S. J. Tang, C. X. Cong, H. Xie, L. Li, H. Xia and T. X. Li, Oriented graphene nanoribbons embedded in hexagonal boron nitride trenches, *Nat. Commun.*, 2017, **8**, 14703.
22 H. S. Wang, L. X. Chen, K. Elibol, L. He, H. M. Wang, C. Chen, C. X. Jiang, C. Li, T. R. Wu and C. X. Cong, Towards chirality control of graphene nanoribbons embedded in hexagonal boron nitride, *Nat. Mater.*, 2021, **20**, 202.
23 D. C. Geng, I. Abdelwahab, X. F. Xiao, A. Cernescu, W. Fu, V. Giannini, S. A. Maier, L. Li, W. P. Hu and K. P. Loh, One-Pot Confined Epitaxial Growth of 2D Heterostructure Arrays, *ACS Mater. Lett.*, 2021, **3**, 217.
24 Y. W. Son, M. L. Cohen and S. G. Louie, Energy Gaps in Graphene Nanoribbons, *Phys. Rev. Lett.*, 2006, **97**, 216803.
25 Y. Matsuda, W. Q. Deng and W. A. Goddard III, Contact Resistance for "End-Contacted" Metal-Graphene and Metal-Nanotube Interfaces from Quantum Mechanics, *J. Phys. Chem. C*, 2010, **114**, 17845.
26 D. M. T. Kuo and Y. C. Chang, Contact Effects on Thermoelectric Properties of Textured Graphene Nanoribbons, *Nanomaterials*, 2022, **12**, 3357.
27 D. M. T. Kuo, Effects of Coulomb Blockade on the Charge Transport through the Topological States of Finite Armchair Graphene Nanoribbons and Heterostructures, *Nanomaterials*, 2023, **13**, 1757.
28 D. M. T. Kuo, Thermal rectification through the topological states of asymmetrical length armchair graphene nanoribbons heterostructures with vacancies, *Nanotechnology*, 2023, **34**, 505401.
29 G. S. Seal and J. Guo, Bandgap opening in boron nitride confined armchair graphene nanoribbon, *Appl. Phys. Lett.*, 2011, **98**, 143107.
30 Y. Ding, Y. Wang and J. Ni, Electronic properties of graphene nanoribbons embedded in boron nitride sheets, *Appl. Phys. Lett.*, 2009, **95**, 123105.
31 Q. F. Sun and X. C. Xie, CT-Invariant Quantum Spin Hall Effect in Ferromagnetic Graphene, *Phys. Rev. Lett.*, 2010, **104**, 066805.
32 X. U. Ning, B. L. Wang, H. Q. Sun and J. W. Ding, Resonance Transmission in Graphene-Nanoribbons-Based Quantum Dot and Superlattice, *Chin. Phys. Lett.*, 2010, **10**, 107303.
33 X. X. Yu and Y. E. Xie, Spin-Polarized transport in graphene nanoribbon superlattices, *Chin. Phys. B*, 2012, **10**, 107202.
34 R. B. Chen, C. P. Chang and M. F. Lin, Electric-field-tunable electronic properties of graphene quantum dots, *Physica E*, 2010, **42**, 2812.
35 T. G. Pedersen, Stark effect and polarizability of graphene quantum dots, *Phys. Rev. B*, 2017, **96**, 115432.
36 J. M. Pruneda, Origin of half-semimetallicity induced at interfaces of C-BN heterostructures, *Phys. Rev. B: Condens. Matter Mater. Phys.*, 2010, **81**, 161409(R).
37 J. Jung, Z. H. Qiao, Q. Niu and A. H. MacDonald, Transport Properties of Graphene Nanoroads in Boron Nitride Sheets, *Nano Lett.*, 2012, **12**, 2936.
38 M. J. J. Mangnus, F. R. Fischer, M. F. Crommie, I. Swart and P. H. Jacobse, Charge transport in topological graphene nanoribbons and nanoribbon heterostructures, *Phys. Rev. B*, 2022, **105**, 115424.
39 D. M. T. Kuo, S. Y. Shiau and Y. C. Chang, Theory of spin blockade, charge ratchet effect, and thermoelectrical behavior in serially coupled quantum dot system, *Phys. Rev. B: Condens. Matter Mater. Phys.*, 2011, **84**, 245303.
40 Y. M. Lee, E. B. Song and T. Hiramoto, Observation of Single Electron Transport via Multiple Quantum States of a Silicon Quantum Dot at Room Temperature, *Nano Lett.*, 2014, **14**, 71.
41 E. Leobandung, L. J. Guo, Y. Wang and S. Y. Chou, Observation of quantum effects and Coulomb blockade in silicon quantum-dot transistors at temperatures over 100 K, *Appl. Phys. Lett.*, 1995, **67**, 938.
42 L. Zhuang, L. J. Guo and S. Y. Choub, Silicon single-electron quantum-dot transistor switch operating at room temperature, *Appl. Phys. Lett.*, 1998, **72**, 1205.
43 H. W. C Postma, T. Teepen, Z. Yao, M. Grifoni and C. Dekker, Carbon Nanotube Single-Electron Transistors at Room Temperature, *Science*, 2001, **293**, 76.